Aeroacoustics Conferences
26-29 May 2026, Brussels, Belgium
32nd AIAA/CEAS Aeroacoustics Conference (2026)

10.2514/6.2026-3408

Numerical Simulations of Rotor Shielding Effects on Axial Flow Fan Using ACTRAN

Manju Adhikary*
École Centrale de Lyon, CNRS, Université Claude Bernard Lyon 1,
INSA Lyon, LMFA, UMR5509, 69130, Écully, France,
AIRBUS OPERATIONS SAS, 316 Route de Bayonne, 31060 Toulouse, France

Antonio Pereira† and Marc C. Jacob‡
École Centrale de Lyon, CNRS, Université Claude Bernard Lyon 1,
INSA Lyon, LMFA, UMR5509, 69130, Écully, France

Ricardo Blázquez-Navarro§ and Stefano Bianchi¶
AIRBUS OPERATIONS SAS, 316 Route de Bayonne, 31060 Toulouse, France

Rotor shielding effects across a low Mach number axial flow fan inside a duct have been studied using the commercial software, ACTRAN. The study investigates spinning azimuthal modes incident on a rotor-stator arrangement with and without flow. The modes are generated using a ring of phased monopole sources representing loudspeakers. Various configurations of the setup have been examined. The effectiveness of rotor shielding, specifically its dependency on frequency, modal spinning direction, and mean flow parameters, has been investigated. The study serves as an extension of a previous experimental campaign conducted on the specific fan geometry. The numerical results have been compared to the experimental outcomes.

I. Nomenclature

A	=	Complex valued Mode amplitudes
c	=	Speed of sound
f	=	Frequency of excitation and analysis
I	=	Identity matrix
K	=	Total number of evenly spaced loudspeakers or monopole sources
$\mathbf{K}, \mathbf{C}, \mathbf{M}$	=	Damping, Stiffness and Mass matrices
k_z, k_r	=	Axial and Radial Wavenumber of modes
k_0	=	Free space wavenumber given by $k_0 = 2\pi f / c_0$
M	=	Flow Mach number
(m, n)	=	Azimuthal and Radial mode order respectively
p	=	Pressure
q	=	Matrix containing unknowns
(r, θ, z)	=	Position in cylindrical coordinate system
t	=	Time parameter
$\mathbf{v}$	=	Velocity vector
(x, y, z)	=	Position in Cartesian coordinate system
η	=	Additive noise
$\mathbf{\Phi}$	=	Acoustic velocity potential
ϕ	=	Loudspeaker phases

*PhD student, Laboratoire de Mécanique des Fluides et d'Acoustique, École Centrale de Lyon and AIRBUS OPERATIONS SAS, manju.adhikary@ec-lyon.fr
†Doctor, Research Engineer, LMFA, École Centrale de Lyon, Écully, France
‡Professor, LMFA, École Centrale de Lyon, Écully, France, AIAA Member
§Aeroacoustics Methods Engineer, Propulsion Physics Department, Airbus Commercial Aircraft
¶Expert in Turbomachinery aeroacoustics, Airbus Commercial Aircraft

ρ	=	Density
ω	=	Angular frequency or pulsations given by $\omega = 2\pi f$

Subscripts and superscripts

$\cdot_0$	=	Mean flow properties
$.'$	=	Acoustic or fluctuating properties
$.^{+/-}$	=	Downstream and Upstream propagating variables respectively
$.^{I,II,III,IV,V}$	=	Microphone array notations

II. Introduction

Fan noise continues to be a major contributor to aircraft noise throughout all phases of operations. Sound generation mechanisms of an aircraft engine and the free-field propagation have been studied extensively [1, 2]. However, analyzing noise propagation within turbofan engines presents unique challenges. The inhomogeneous and swirling flows inside the engine create intricate noise generation and propagation pathways. Specifically, forward-radiated noise from the rotor-wake-stator interaction, creating Tyler and Sofrin modes [3], propagates across the rotor prior to exiting the engine. Consequently, improving the knowledge of noise transmission through the rotor blades is critical for developing more precise noise assessments. Kaji and Okazaki [4, 5] introduced one of the earliest analytical frameworks for examining noise transmission through stationary rotor blades, which models the blades as an infinite array of two-dimensional flat plates characterized by a finite chord length and negligible thickness. The transmission and reflection of acoustic energy are significantly affected by the propagation angle of the modes. However, such models have been validated for plane modes only at low frequencies. Philpot [6] extended the long-wavelength theory to three dimensional blades and compared the analytical results to experimental trends, showing that high rotor Mach numbers and counter-rotating modes significantly increase noise attenuation. Posson and Moreau [7] incorporated quasi-3D rotor model of acoustic broadband noise shielding and frequency scattering effects within an annular duct. Results show that rotor shielding decreases upstream acoustic power at intermediate frequencies but increases at higher frequencies due to frequency scattering and radial mode redistribution. More recently, the acoustic shielding of broadband noise by fan rotors has been investigated using linearized frequency-domain Navier-Stokes solvers and a strip-wise approach to demonstrate up to 9 dB rotor blockage at high-speed conditions, primarily due to supersonic pockets and shock waves [8]. Such observations cannot be accurately captured by standard flat-plate approximations.

In the present study, the authors attempt to conduct a comprehensive study of acoustic shielding of tonal noise across a rotor-stator row. An academic case involving a Heating, ventilation and air-conditioning (HVAC) fan with a single rotor-stator row was previously investigated [9]. The present study extends this investigation by performing noise transmission studies across fan blades using Actran: a finite element-based software for modeling sound propagation, transmission and absorption in acoustic, vibro-acoustic, or aero-acoustic scenarios. The finite element code Actran/TM has been employed for non-rotating fan configurations, while the rotating cases are modeled using the Discontinuous Galerkin method-based Actran DGM. Actran/TM has been in extensive use for industrial applications as well as academic research. On the contrary, very few studies have been performed using Actran DGM, even less so with a rotating component. One of the recent studies is the simulation of installation effects of Aircraft Engine Rear Fan noise and comparison against experimental observations [10]. A good agreement has been observed in spite of some uncertainty in the source level and inaccuracies in the model due to spurious reflection on the domain border. The current investigation further explores the capabilities of the DGM approach for complex rotating machinery and aeroacoustic propagation problems. The experimental setup and numerical modeling are presented in Sec. III. The results and comparison of transmission loss across fan stages for different modes are demonstrated in Sec. IV. Finally, a brief summary of the study and the advantages and limitations of the software are discussed.

III. Experimental setup and Numerical modeling

The experimental setup consists of a cylindrical duct with a radius of 0.085 m. A low-speed electrical HVAC fan, designated LP3, manufactured by Safran Ventilation Systems is installed inside the duct. The most relevant parameters of LP3 are listed in Table 3.

Table 3 Parameters of LP3 used in experimentation and numerical simulations

Rotor blades number	B	17
Stator vanes number	V	23
Diameter	D	17 cm
Hub to tip ratio	R_H/R_T	0.55
Tip Mach number	M_{tip}	0.3
Maximum rotational speed	Ω_{max}	~ 10000 rpm
Maximum mass flow rate	Qm	~ 1 $kg\ s^{-1}$
Maximum mean axial flow velocity	U_0	~ 40 $m\ s^{-1}$

A ring of 13 loudspeakers downstream of LP3 generate specific azimuthal modes inside the duct based on their relative phase difference. A particular spinning mode can be generated inside a duct using a combination of phased loudspeakers with the relative phase of the j-th loudspeaker is given by ([11, 12]):

$$\phi_j = \frac{2\pi m}{K}(j-1) \tag{1}$$

The acquisition system comprises 2 sets of 25 pin-hole-mounted 1/4" microphones, respectively upstream and downstream of the fan and 64 remotely mounted 1/4" microphones in the interstage section. Figure 1 sketches a representation of the experimental setup. The fan is operated at 9800 rpm, resulting in a relative tip Mach number of 0.3. The number of loudspeakers used for mode generation limits the maximum mode number that can be excited without aliasing (half of the number of loudspeakers according to the Shannon-Nyquist criterion). Consequently, modes ranging from $m = -6$ to $m = +6$ are selected for the experimental campaign. Mode generation consists pure tones excited individually at 30 frequencies between 500 Hz and 10000 Hz for each azimuthal mode.

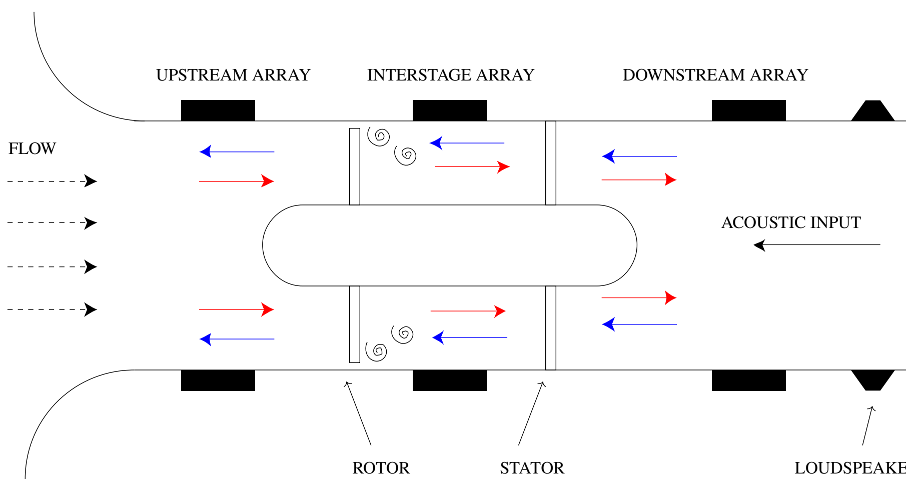

Fig. 1 Schematic diagram of the experimental setup showing the positions of microphone antenna and direction of acoustic wave propagation. Blue arrows depict the incident direction of modes i.e. the same direction as that of acoustic input, and the red arrows depict the reflected direction of mode propagation

A. Static simulations : ACTRAN/TM

The numerical simulations replicate the conducted experiments and are performed for the azimuthal modes and frequencies corresponding to the experimental test matrix. Two different methodologies have been adopted: static and rotating. Static configurations modeling the LP3 but with no rotation of blades or flow inside the duct are simulated and analysed using ACTRAN/TM Direct frequency response analyses. Several different configurations are simulated as presented in Table 4.

Table 4 Different configurations of the setup studied in numerical simulations

Configuration Id	Description	Rotational speed	Flow	Solver
A	Empty cylindrical duct	-	-	ACTRAN/TM
B		9800 rpm	-	ACTRAN DGM
C	Duct with hub	-	-	ACTRAN/TM
D	Duct with hub and stators	-	-	ACTRAN/TM
E	Duct with hub and rotors	-	-	ACTRAN/TM
F	Full LP3 configuration	-	-	ACTRAN/TM
G		-	-	ACTRAN DGM
H		9800 rpm	-	ACTRAN DGM
I		-	Uniform axial flow M=0.1	ACTRAN DGM
J		9800 rpm	Flow from CFD	ACTRAN DGM

Meshing has been performed on ANSA from BETA simulation solutions. Preference has been given to linear quadrilateral elements except at the proximity of the fan. Meshing has been maintained symmetric about the duct axis as much as possible. Linear quadrilateral elements have been found to perform better in interpolation and convergence. The elements near the rotor and stator blades are refined and changed to triangles to follow the geometry and avoid distortion. Two different meshes are generated: one for frequencies up to 5000 Hz and another one from 5000 Hz to 10000 Hz with a minimum of 4 elements per wavelength in each case. The loudspeakers are represented using 13 monopole sources which are basically three dimensional spherical sources of given pressure amplitude. The monopole sources accurately represent the loudspeakers, since in the experimental setup they are connected to the duct by thin waveguides with a much higher cut-off frequency (14240 Hz) thus generating only plane waves. To excite a particular mode, the sources have a phase difference calculated using Eq. 1. The duct ends are modeled using a feature known as "Modal ducts" which models a semi-infinite duct where the modal amplitudes of the reflected modes are set to zero. The fundamental equation to be considered for acoustic propagation in straight walled ducts with a uniform axial flow is the convected wave equation in cartesian coordinates:

$$\frac{\partial^2\Phi}{\partial x^2} + \frac{\partial^2\Phi}{\partial y^2} + (1 - M^2)\frac{\partial^2\Phi}{\partial z^2} - 2ikM\frac{\partial\Phi}{\partial z} + k^2\Phi = 0 \tag{2}$$

The equation is expressed in terms of the velocity potential Φ. The potential formulation is more computationally efficient for irrotational and homentropic mean flows. The acoustic pressure and the velocity vector are related to the velocity potential by

$$p' = -\rho_0 c_0 (ik\Phi + M\frac{\partial\Phi}{\partial z}) \tag{3}$$

$$\mathbf{v}' = \nabla\Phi \tag{4}$$

In the direct frequency response analysis, following system of equations is solved in the frequency domain for given pulsations ω using Finite Element Scheme [13]:

$$(\mathbf{K} + i\omega\mathbf{C} - \omega^2\mathbf{M})\mathbf{q}(\omega) = \mathbf{F}(\omega) \tag{5}$$

To create a parallel with the convected wave equation, the unknown $\mathbf{q}(\omega)$ is the velocity potential Φ. The forcing term comes from excitations (point sources or incident modes) and the stiffness, damping, and mass-like matrices depend on wall boundary conditions, mean flow, and acoustic wavenumber at the frequency of analysis. The advantage of Direct frequency response analyses is that, multiple excitation frequencies can be provided in a single analysis and results will be saved for each individual frequency excitation. The problem is steady-state, so standard convergence acceleration techniques can be employed. Further, the computation can be parallelised in frequency to achieve shorter run time. However, it is not able to handle the rotating blades and is only suitable for static cases.

B. Rotating simulations : ACTRAN DGM

In order to model a rotating fan, ACTRAN DGM is used since it allows the incorporation of a rotating component. ACTRAN DGM solves the unsteady linearized Euler equations in the time domain, using a Discontinuous Galerkin space discretisation [14]. The Homentropic Linearized Euler equations are given by:

$$\frac{\partial \rho'}{\partial t} + \nabla.(\rho \mathbf{v})' = 0 \tag{6}$$

$$\frac{\partial (\rho \mathbf{v})'}{\partial t} + \nabla.[(\rho \mathbf{v})' \otimes \mathbf{v}_0 + \mathbf{v}_0 \otimes (\rho \mathbf{v})' + \rho'(c_0^2 \mathbf{I} - \mathbf{v}_0 \otimes \mathbf{v}_0)] = 0 \tag{7}$$

The general form of the equations for the j-th element considered in ACTRAN DGM is the following [13]:

$$\frac{\partial q}{\partial t} + \frac{\partial}{\partial x_j}(F_j.q) = 0 \tag{8}$$

where the values of F_j contain local mean flow information and q is a vector where all unknowns are stored element-wise. The mass, momentum and energy equations are multiplied by the Galerkin shape functions N_α associated to the elements and integrated across the volume and surface of each element:

$$\int_\Omega N_\alpha \frac{\partial q}{\partial t} dV = \int_\Omega \frac{\partial N_\alpha}{\partial x_j} F_j.q dV - \oint_{\partial\Omega} N_\alpha F_j.q n_j dS \tag{9}$$

The element boundary integrals are computed by considering the solution in the two adjacent elements. The special feature of Discontinuous Galerkin is that the solution can be different on the two sides of an element face and the continuity is not enforced by nature as for classical finite element methods. Therefore, it is important to carefully select Plane tolerance and Convergence check tolerance values. Plane tolerance defines the geometric precision for identifying parallel faces and boundary alignments, while Convergence check tolerance sets the numerical threshold for terminating iterative solver loops once the solution error is sufficiently small. Figure 2 shows the setup as modeled for numerical simulations. A part of the duct including the rotors rotates at 9800 rpm. The rotating interface upstream is in the circular section of duct and the interface downstream is equally spaced between the rotors and stators. The interfaces share the same mesh from static to rotating domain and continuity is maintained. The interstage microphone array has been divided into two parts: one half in the static domain (Array II) and the remaining half in the rotating domain (Array III). Another set of microphones has been added upstream of rotor (Array IV) to inspect the upstream rotating interface. The array contains 32 microphones, same as that of interstage arrays, and is not present in the actual experimental setup. The microphones in the rotating domain have been provided with a pseudo-negative rotational speed in order to extract the pressure amplitudes in static frame of reference. DGM simulations support only triangular elements on the surfaces and tetrahedral elements in the volume. A preliminary mesh has been created in ANSA with uniform and axisymmetric hexahedral elements. The elements are then converted to tetrahedrons using ACTRANVI. Regardless of the recommendation to have the element size as 1.5 times the wavelength, the meshing is dictated by blades geometry and duct perimeter in order to respect the geometrical tolerances, which are more constraining than the acoustic criterion. In this case, the duct ends are modeled using "Buffer" component with Non-reflecting boundary conditions at ends. This condition enforces that all the incoming modes normal to the boundary are set to zero and the outgoing modes are smoothly damped throughout the buffer length. For the simulations in the study, the buffer thickness is chosen to be 1.5 m in accordance to the largest wavelength of excitation.

For a preliminary study of the flow effects, a uniform flow of Mach number 0.1 is applied throughout the duct. The Mach number reflects the flow in the duct when the fan rotates at 9800 rpm. This configuration is referred to as "M=0.1" hereafter. Computations featuring rotating blades require an accurate modeling of the flow, since it significantly impacts the propagation of acoustic waves. To simulate such conditions, the mean flow around the LP3 fan is characterized via Computational Fluid Dynamics (CFD), using the elsA solver [15] on a structured grid generated via Autogrid. The domain consists of a single rotor and stator passage with periodic boundary conditions applied at the lateral boundaries. To obtain a steady-state solution, a mixing-plane interface is positioned between the rotor and stator, matching the location of the rotating interface used in the subsequent ACTRAN DGM computation. Turbulence is modeled using the kLSmith RANS approach [16]. The hub and shroud were treated as inviscid boundaries to prevent numerical instabilities within ACTRAN DGM. While the Mixing-Plane approach introduces a flow discontinuity by averaging out rotor wakes, this simplification is justified by the low mean flow Mach number and the small scale of the wakes relative to the acoustic frequencies investigated. Finally, the base flow is reconstructed over 360 degrees and interpolated onto the acoustic

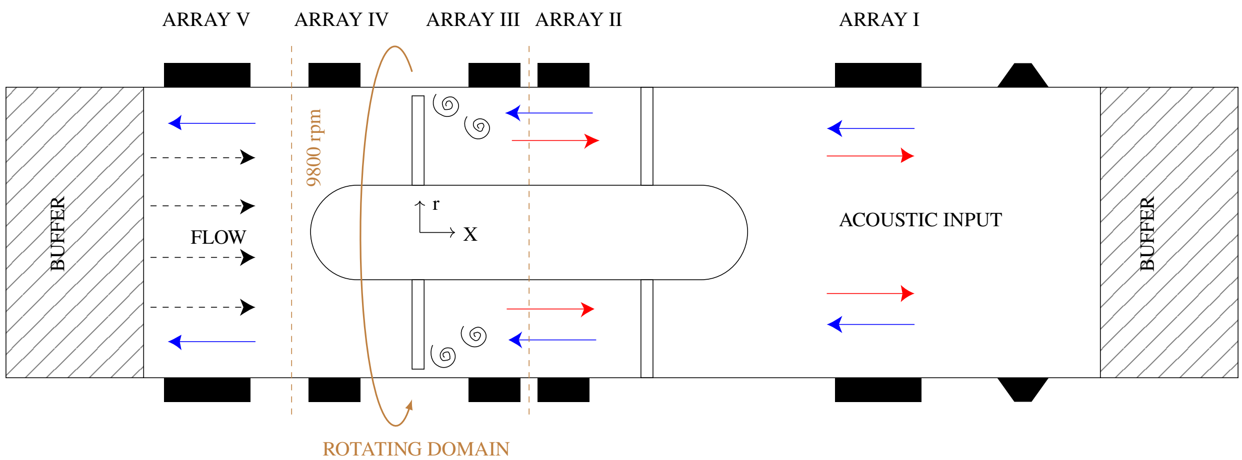

Fig. 2 Schematic diagram of the setup as modeled in the numerical simulations showing the positions of microphone antenna, the rotating domain and direction of acoustic wave propagation, blue arrows depict the incident direction of modes, i.e. the same direction as that of acoustic input and the red arrows depict the reflected direction of mode propagation

mesh using Actran iCFD. The flow inside the buffer regions is set as a constant with the axial velocity matching that of the generated flow using CFD at duct ends. The time discretisation is performed by an explicit finite difference scheme, typically a 4th order Runge-Kutta scheme. MUMPS(Multifrontal Massively Parallel Solver) is used in both Actran/TM and DGM as it is available for both frequency and spatial parallelisation [17]. It is a high-performance numerical library designed to solve large systems of sparse linear equations using a direct multifrontal method and is widely used in Finite Element softwares.

C. Post-processing

The microphones are modeled in the numerical setup to precisely match their actual experimental positions. The pressure values captured at these microphone positions are fed into the iterative Bayesian Inverse Approach (iBIA) to calculate the mode amplitudes at each array location [18]. Assuming linear acoustics behavior and a stationary sound field, the complex acoustic pressure inside a hard-wall cylindrical duct with a circular or annular cross-section and in the presence of a flow, can be expressed as a weighted sum of modes [19]:

$$p(r,\theta,z,t) = \sum_{m=-\infty}^{\infty}\sum_{n=0}^{\infty}[A^+_{mn}e^{ik^+_{z,mn}z} + A^-_{mn}e^{ik^-_{z,mn}z}]f_{mn}(r)e^{im\theta}e^{i\omega t} \tag{10}$$

$$k^{\pm}_{z,mn} = \frac{\mp Mk_0 + \sqrt{k_0^2 - (1-M^2)k^2_{r,mn}}}{1-M^2} \tag{11}$$

Equation 10 can be represented in a matrix notation.

$$\mathbf{p} = \mathbf{\Psi}\mathbf{q} + \eta \tag{12}$$

where, $\mathbf{q}$ contains the unknown complex coefficients $A^{\pm}_{mn}$, and $\mathbf{\Psi} = e^{ik^{\pm}_{z,mn}z}f_{m,n}(r)e^{im\theta}$ in this case. The unknowns $\mathbf{q}$ and observations $\mathbf{p}$ (result of a Fourier transform from microphone data) are considered as random variables which are modeled through probability density functions and an algorithm based on the majorisation–minimisation (MM) principle is employed to solve the problem [18]. In addition to microphone data, volume maps containing the frequency-domain or temporal solutions of pressure, velocity and density are recorded which can be used for visualisation. Moreover, the pressure and velocity values can be extrapolated from the maps, at a grid of points on the section and used for mode decomposition either using iBIA method or Eigenmode decomposition [20].

IV. Results

From the pressure values at microphone positions amplitudes of all the modes present at corresponding duct location are calculated using the post-processing methodology explained above. The mode amplitudes can then be used to compute the acoustic power of modes. Results are presented in Sound pressure levels and Sound power levels with reference values of $p_{\mathrm{ref}} = 2 \times 10^{-5}$ Pa and $W_{\mathrm{ref}} = 10^{-12}$ W. The variations in these acoustic quantities are analyzed as a function of the reduced frequency $2\pi f R_T / c_0$, to highlight the modal behavior relative to the duct dimensions. The presented set of results corresponds to excitation of azimuthal mode $+1$ and -1. The +ve sign represents co-rotating modes and the -ve represents counter-rotating modes with respect to the rotor rotation. The overall transmission loss can be obtained by taking the difference of incident mode power at upstream array from that at downstream array i.e. Array I-Array V in Fig. 2. Higher difference in mode power means stronger shielding, while -ve difference may indicate a gain in acoustic power. Figure 3 is the pictoral representation of spinning mode -1 at the downstream array location excited at 3500 Hz.

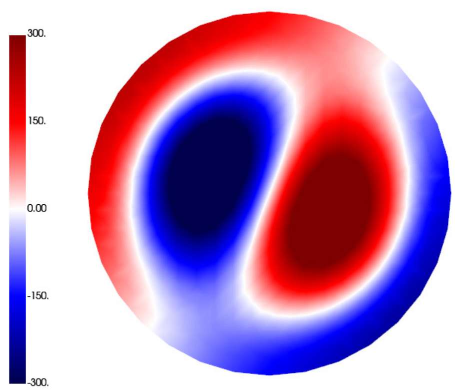

Fig. 3 Acoustic pressure map (Pa) in the duct section at Array I upon excitation of azimuthal mode -1 at 3500 Hz representing the spinning mode

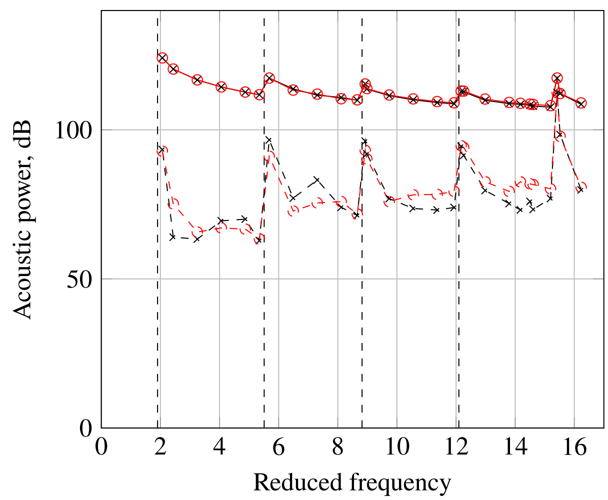

Fig. 4 Acoustic power of azimuthal mode -1 (summed for all cut-on radial modes) along incident (solid) and reflected (dashed) direction for Array V(o-red) and Array I(x-black) inside an empty cylindrical duct - Conf. A in Table 4- (dashed vertical lines represent the cut-off frequencies of subsequent radial modes)

The first set of tests is performed on an empty cylindrical duct without rotation or flow. The microphone arrays remain at the same position as in Fig. 2. Figure 4 presents the acoustic power of azimuthal mode -1 along the incident and reflected directions, as recorded by the microphone arrays I and V. The measured acoustic power is conserved across the microphone arrays, which aligns with theoretical predictions. This consistency is especially strong at low frequencies where few radial order modes are propagating. However, sharp increases in sound power are noted near the cut-off frequencies of higher-order radial modes. This is because near cut-off, mode excitation is highly sensitive and manifests as high-magnitude resonance, a common phenomenon in duct acoustics. The acoustic power of the reflected mode is considerably lower than that of the incident mode. Similar observations have been made for the other azimuthal modes. These comparable results provide confidence in the methodology used for sound generation and post-processing. To complement these results, the mode amplitudes are also computed using ACTRAN utility iTM, employing the Single Plane Pressure Velocity (SPPV) method [13]. The iTM utility in ACTRAN uses the pressure and velocity values across a defined plane to compute the amplitudes of incident modes at that location. The planes are chosen at the positions of the microphone arrays. Figure 5 presents the power of azimuthal mode -1 along incident and reflected directions at different microphone array positions. The powers obtained by the two methods, microphones post-processing and ACTRAN iTM, superimpose, thereby validating the methodology used.

One of the interests in performing numerical simulations is to enable the modeling of scenarios that are not experimentally feasible. These configurations help to isolate the effects of each individual components inside the duct

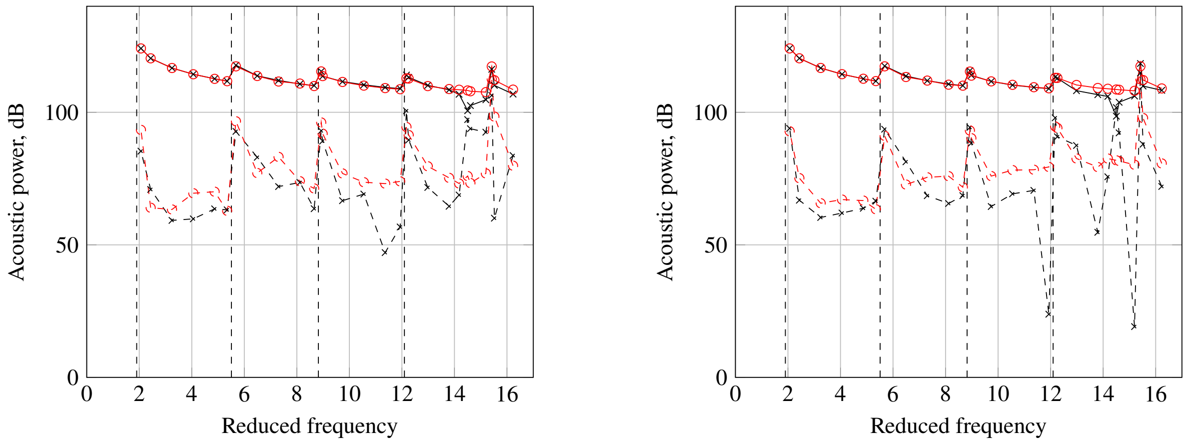

(a) Array I **(b) Array V**

Fig. 5 Acoustic power of azimuthal mode -1 (summed for all cut-on radial modes) along incident (solid line) and reflected (dashed line) direction in the case of an empty circular duct- Conf. A in Table 4- calculated using microphone post-processing (x-black) and ACTRAN ITM (o-red) (dashed vertical lines represent the cut-off frequencies of subsequent radial modes)

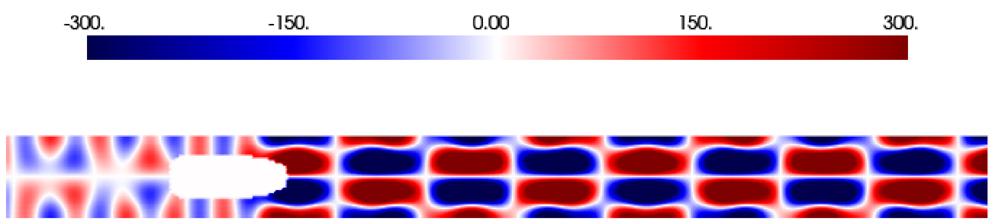

Fig. 6 Acoustic pressure map (Pa) across the midplane inside the duct with only the hub of LP3 present and excitation of azimuthal mode -1 at 3500 Hz-Conf. C in Table 4

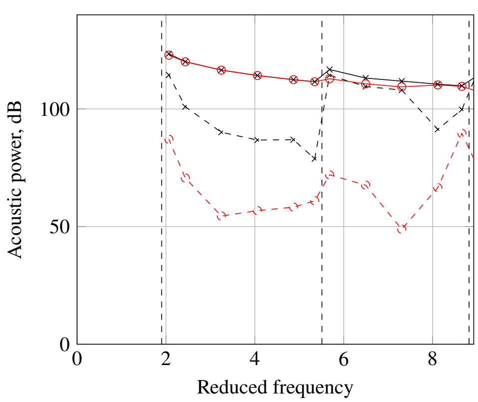

Fig. 7 Acoustic power of azimuthal mode -1 (summed for all cut-on radial modes) along incident (solid) and reflected (dashed) direction for Array V (o-red) and Array I (x-black) in the case of circular duct with hub- Conf. C in Table 4 (dashed vertical lines represent the cut-off frequencies of subsequent radial modes)

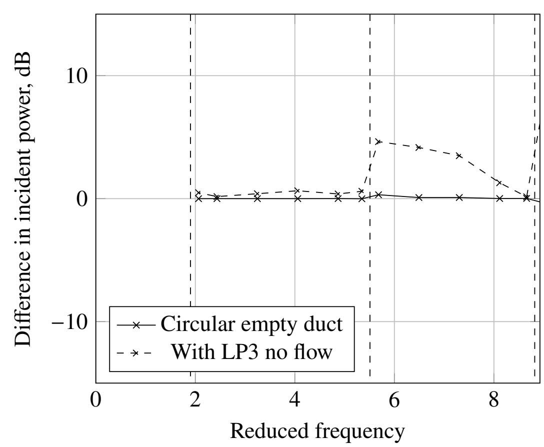

Fig. 8 Difference in acoustic power along incident direction (Array I-Array V) of azimuthal mode -1 (summed for all cut-on radial modes) for Conf. A and Conf. F from Table 4 (dashed vertical lines represent the cut-off frequencies of subsequent radial modes)

and their effect on mode propagation, for example the impact of cylindrical to annular transition due to the hub. The impact of the hub on noise transmission has been numerically investigated in a dedicated analysis. The domain consists of a floating hub, with neither stators nor rotors. Figure 6 shows the acoustic pressure map at the midplane of the duct with hub when azimuthal mode -1 is excited at 3500 Hz. At this frequency, mode $(-1, 1)$ is propagating in the circular section and cut-off in the annular section. It can be observed that not only does the mode pattern change at the transition but also the pressure amplitude decreases significantly. Even though mode $(-1, 0)$ is present throughout, mode $(-1, 1)$ carries more energy as it is closer to its cut-off frequency and thus leads to decrease in overall energy when it is cut-off. This phenomenon can also be observed by plotting acoustic power of azimuthal mode -1 along reduced frequency (Fig. 7). The incident mode power at the Array V decreases between 3500 Hz and 4500 Hz while the reflected mode power at Array I is high in this range. This effect remains consistent even when the full LP3 configuration is simulated. Figure 8 shows the transmission loss of azimuthal mode -1 with frequency for empty duct and duct with LP3. In this case, the fan is static and the effects of blade rotation and flow are not taken into account. The presence of LP3 decreases the transmission of azimuthal mode $(-1, 0)$ by 0.6 dB, which is the only mode present until 3394 Hz. Beyond this frequency, the next order radial mode $(-1, 1)$ is propagating. The transmission loss is higher due to cylindrical to annular transition

To further understand the influence of each component of the setup, different configurations as mentioned in Table 4, are simulated for static cases, i.e. neither the fan rotates, nor there is flow inside the duct. Mode (1,0) is excited and the frequency is limited such that only the first radial mode propagates inside the duct. The difference in acoustic power of incident mode between downstream and upstream arrays of microphones (Array I-Array V) provide the shielding due to each of these components and are plotted in Fig. 9a. It can be observed that the incident power remains unchanged for the empty cylinder, also verified from previous plots. The presence of hub and stators cause a slight increase in shielding for the particular mode specially at higher frequencies. The stators cause low shielding owing to their low stagger angles. It is also evident that the rotors are more effective in shielding the incident mode. The combined effect of both rotors and stators lead to a stronger shielding, which increases with frequency until 3000 Hz.

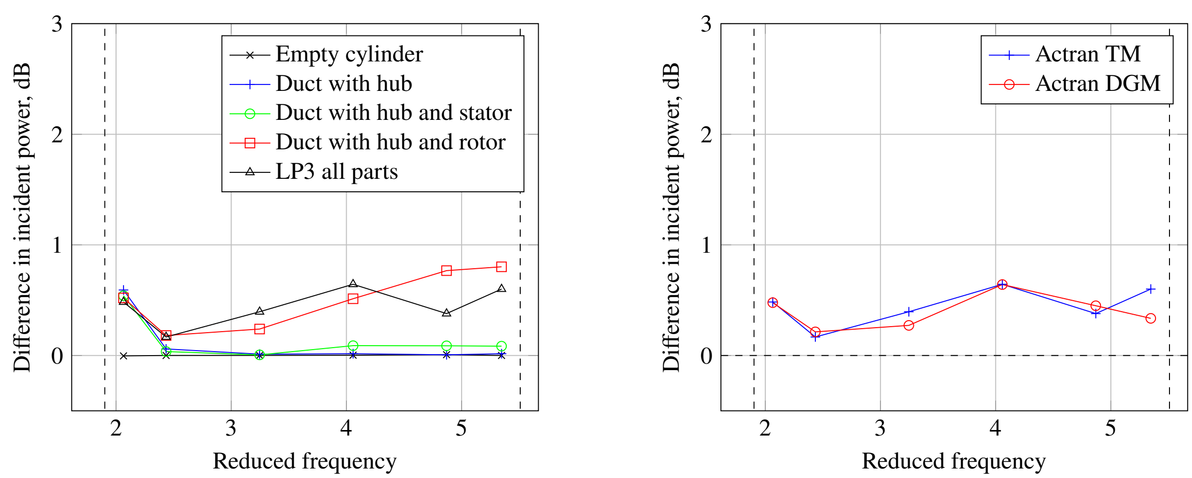

(a) Different configurations using ACTRAN/TM (Conf. A & Conf. C-F in Table 4)

(b) Full LP3 configuration ACTRAN/TM vs DGM (Conf. F & Conf. G in Table 4)

Fig. 9 Difference in acoustic power along incident direction Array I-Array V of mode (1,0) for different static configurations (dashed vertical lines represent the cut-off frequencies of subsequent radial modes)

In order to simulate more accurately the complete configuration, i.e. LP3 with rotating blades and flow generated from CFD simulations, ACTRAN DGM is used. The following results are obtained from the post-processing of the ACTRAN DGM simulations. For verification purposes, a static configuration is first analysed with neither rotation nor flow. Figure 9b demonstrates that the estimation of acoustic shielding of mode (1,0) across static LP3 using ACTRAN DGM is in close agreement with ACTRAN/TM. Subsequently, the analysis is extended to the complete LP3 configuration, wherein both blade rotation and CFD flow effects are incorporated. Four different post-processing methods are compared and presented in Fig. 10. Simulations correspond to full LP3 configuration with rotating domain and CFD flow. From the simulations, the pressure field is recorded on the three dimensional mesh for each time interval. ACTRAN iTM utility is applied on planes at the position of the microphone antenna. The static and fluctuating values of parameters across 1100 points on each of the planes are extrapolated and fed into an inhouse numerical acoustic modal decomposition solver, recently developed at Airbus, with uniform, isentropic and inviscid flow assumptions. The method is similar to that implemented by Law et al. [20]. For the next two post-processing methods, the microphones are modeled in the numerical simulation and the pressure time signal at these positions are recorded. The time taken by the acoustic mode to arrive at the duct end plus two complete fan revolutions is considered the transient part of signal and removed from the Fourier transform calculation. Part of time signal corresponding to 12 times fan rotation is then used for mode decomposition. Discrete Fourier Transform (DFT) is calculated using iCFD DFT utility available in ACTRAN or using MATLAB before applying mode decomposition using iBIA method [18]. The difference in power of excited mode between the upstream and downstream array provides an estimate of transmission loss across the fan. It is observed that the microphones post-processing overestimate the transmission loss as compared to Eigenmode decomposition and ACTRAN iTM. The microphone data consist of values only on the duct surface while iTM and Eigenmode decomposition include information in the section as well. Both the different Fourier transforms, even though providing slightly different estimates of absolute power values, have superimposing values of transmission loss. Nevertheless, all the methods show similar trend for both co-rotating and counter-rotating modes. For further analyses, the microphone post-processing algorithm based on iBIA and using DFT from ACTRAN is used in order to facilitate comparison with results from ACTRAN/TM and experiments.

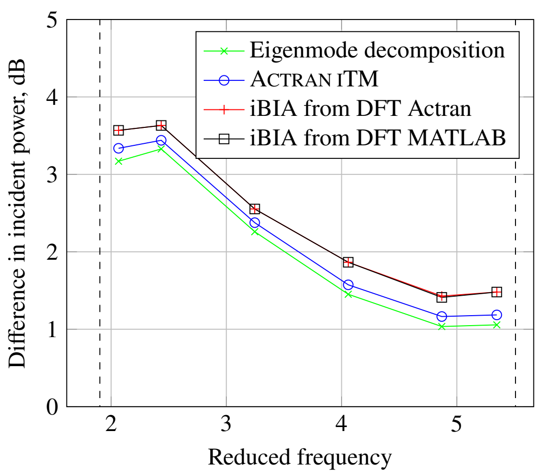

(a) Mode (1,0)

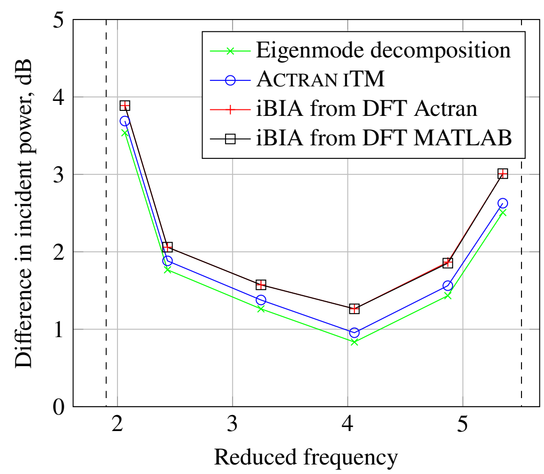

(b) Mode (-1,0)

Fig. 10 Difference in acoustic power along incident direction Array I-Array V across LP3 with rotation and CFD flow comparing different post-processing methods from DGM simulations-Conf. J in Table 4 (dashed vertical lines represent the cut-off frequencies of subsequent radial modes)

The difference in power of excited mode across each position of the setup is plotted in Fig. 11 for both co-rotating and counter-rotating mode. It is to be noted that a loss or gain of acoustic intensity across the interfaces (dashed lines) has been observed. Also, the reflection from the interface leads to an increase in the reflected acoustic intensity in the interstage region, further enhanced by reflection from the stators. This effect is particularly remarkable for the counter-rotating mode as observed by negative values of shielding across stators. The change in acoustic intensity across the interfaces and spurious reflections modify the overall shielding across the fan notably at low frequencies. This effect can also be observed by performing a similar analysis on an empty cylindrical duct with a part of the mesh rotating at 9800 rpm (Fig. 12). Differences in acoustic power across successive microphone arrays provide the transmission loss related to each interface. As shown in Fig. 13, there is a loss of acoustic intensity across the downstream interface and a gain in acoustic intensity across the upstream interface. The total difference, ought to be zero, is considerably high at low frequencies and while seeming to cancel each other at higher frequencies is never null. This is a major limitation of the numerical setup, mainly because the loss or gain of acoustic intensity is not consistent across frequencies, modes, or even configurations, and is of the same order as the investigated phenomenon. To overcome this drawback in the numerical simulations, instead of taking the total difference of power of incident mode between Array I and Array V, the shielding is calculated by adding individual shielding values across rotors (Array III-Array IV) and stators(Array I-Array II). This hypothesis itself has some relevant limitations, notably the fact that reflections from the interfaces followed by second-order reflections may pollute the shielding values. Also, the interface may change the relative content and phase of the different radial modes, and can lead to differences in the sound transmission. This effect is not prominent in the presented results, as in the considered range of the frequencies only first radial mode is cut-on.

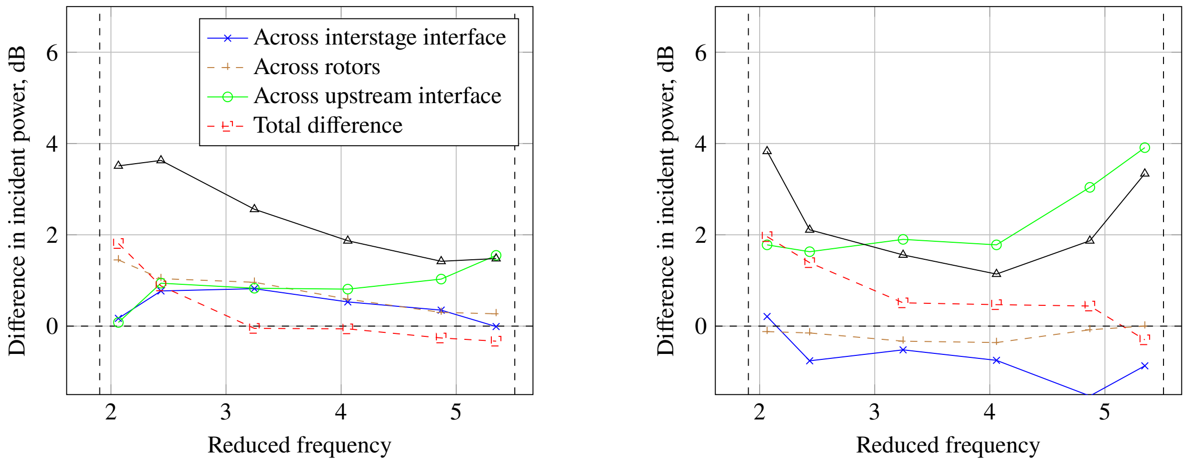

(a) Mode (1,0) **(b) Mode (-1,0)**

Fig. 11 Difference in acoustic power along incident direction across different positions of the setup with effects of fan rotation and CFD flow-Conf. J in Table 4- (a)Across stators = Array I-Array II (b)Across interstage interface = Array II-Array III (c)Across rotors = Array III-Array IV (d)Across upstream interface = Array IV-Array V (e)Total difference=Array I-Array V(dashed vertical lines represent the cut-off frequencies of subsequent radial modes)

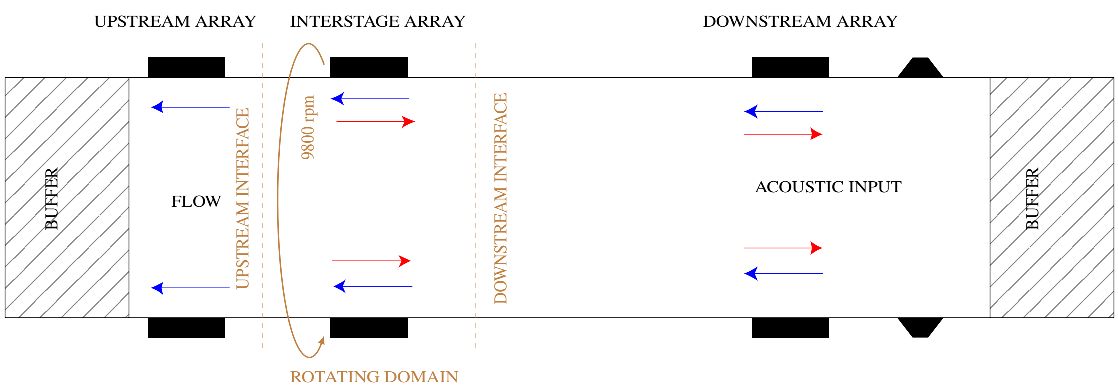

Fig. 12 Schematic diagram of the empty cylindrical duct (Conf. B) as modeled in Actran DGM. Blue arrows depict the incident direction of modes, i.e. the same direction as that of acoustic input and the red arrows depict the reflected direction of mode propagation

Figure 14 shows the effect of rotation and flow on shielding across LP3 for mode (1,0). In the case of simulations with rotating component, instead of taking the overall transmission loss values, shielding across rotors and stators are taken individually and added as discussed before. The presence of non-rotating LP3 (also verified in Figs. 9a and 9b) causes shielding of about 0.5 dB specially beyond 2500 Hz. Adding a constant axial flow of M=0.1 inside the duct increases the shielding by around 1.4 dB throughout the range of frequencies. The fan rotation leads to high shielding at low frequencies, which then decreases at higher frequencies. The full simulation includes a rotating fan incorporating flow generated from a CFD simulation. The overall shielding increases from 1272 Hz to 1500 Hz and then remains almost constant. Figure 15 presents the shielding across the fan including fan rotation and flow effects, obtained from numerical simulations as compared to that obtained from experimental campaign [9]. The experimental results align better with shielding across the rotor than overall shielding. This can be explained from the former observations where shielding across the stators is incorrectly estimated due to the reflection caused by the interface. Moreover, it has been stated from static simulations that the stators play minimal role in blocking mode (1,0) and (-1,0) because of their low stagger angles.

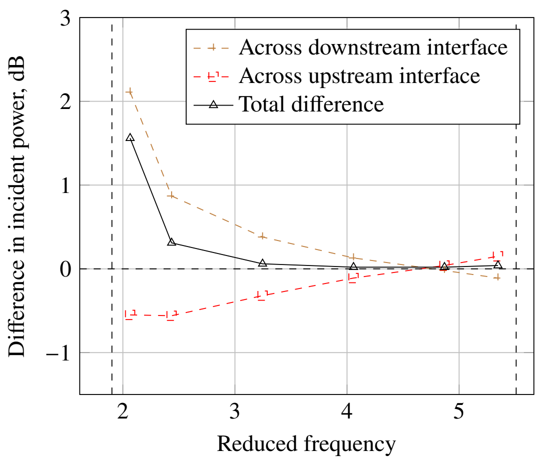

Fig. 13 Difference in acoustic power along incident direction across different positions of a cylindrical duct with rotating domain in DGM simulations-Conf. B in Table 4- (dashed vertical lines represent the cut-off frequencies of subsequent radial modes)

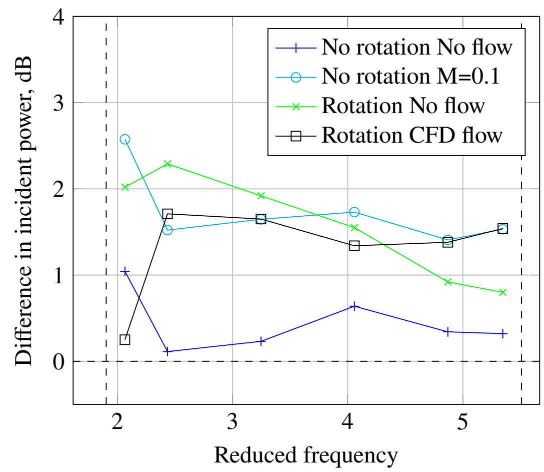

Fig. 14 Total shielding across the fan of incident mode (1,0) showcasing the effects of flow and fan rotation from DGM simulations-Conf. G-J in Table 4- (dashed vertical lines represent the cut-off frequencies of subsequent radial modes)

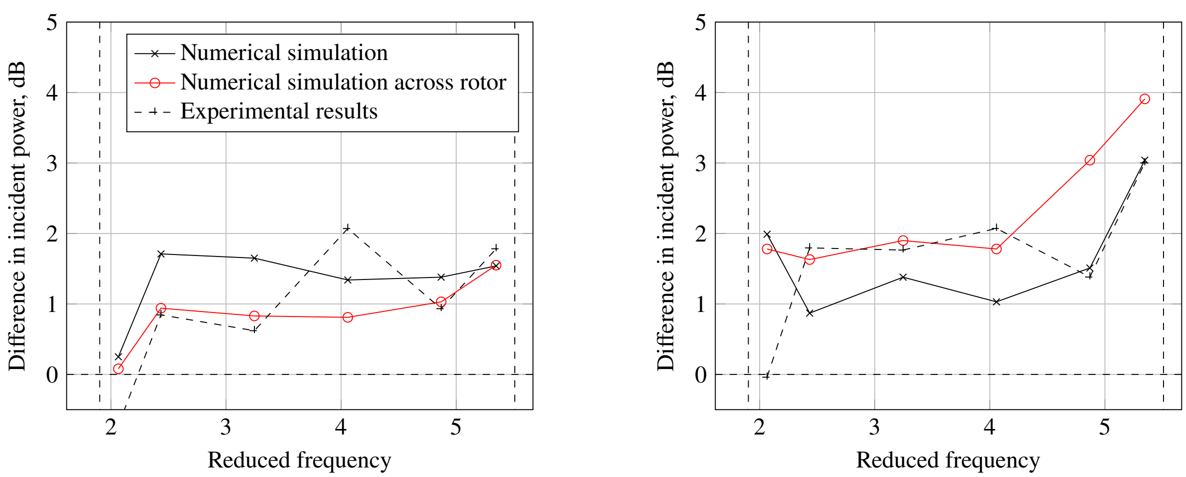

(a) Mode (1,0)

(b) Mode (-1,0)

Fig. 15 Difference in acoustic power along incident direction of Array I-Array V across LP3 with effects of fan rotation and flow comparing DGM simulations-Conf. J in Table 4- with experimental observations [9], Red line shows shielding across rotors (Array III-Array IV) (dashed vertical lines represent the cut-off frequencies of subsequent radial modes)

V. Conclusion and Discussion

A fully functional, low speed HVAC system fan inside a duct has been simulated using commercial software ACTRAN to characterize the acoustic shielding effects. ACTRAN/TM has been employed for static simulations with no blade rotation or flow, whereas ACTRAN DGM has been used for modeling blade rotation and complex flow. The methodology to simulate the experimental setup in static configurations and to estimate the fan shielding effect is validated by verifying that the acoustic intensity remains constant across a cylindrical duct. Different post-processing methods have been compared with results showing a consistent trend. Static simulations reveal several important observations, for instance, the rotors are more effective in shielding mode $(\pm 1, 0)$ than other components, while stators are almost transparent to modes ± 1. Counter-rotating modes are shielded more effectively than co-rotating modes. Furthermore, at certain frequencies, the effect of a mode propagating in the circular section and cut-off in the annular section can be observed. This leads to loss in incident power of the mode upstream of the fan. Static simulations in ACTRAN DGM provide satisfactory results matching quite well with ACTRAN/TM static simulations. However, incorporating rotating domain inside the mesh leads to loss in acoustic intensity and spurious reflections at the static and rotating component interfaces. One way to isolate the effect of interfaces is to look at shielding at each individual component and add them a posteriori. However, this method is not foolproof since the reflections from the interfaces can get doubly reflected from stator edges and pollute the mode power estimations. Nonetheless, important conclusions can be drawn from the simulations. The presence of flow increases shielding considerably and is a dominant factor in shielding estimations. The Rotation of the blade increases shielding at low frequencies. The results have been compared to experimental observations from literature involving the same fan geometry. The shielding observed in the experimental campaign matches more closely to that across rotors in the simulations rather than the complete LP3 which includes stators' influence as well.

While the results provide a fundamental understanding of rotor shielding, addressing the inconsistencies at the rotating interfaces remains a priority for refining future predictive models. The interface of the rotating domain in ACTRAN DGM is currently being refined to mitigate non-physical intensity loss. Simultaneously, different analysis criteria are discussed to isolate such effects. Numerical and experimental studies are currently underway to further explore acoustic shielding due to excitation of higher order azimuthal and radial modes. As higher frequencies are approached, the presence of concurrent radial and azimuthal modes introduces significant complexity. In this regime, frequency and modal scattering are anticipated, leading to intricate trends in fan shielding and acoustic reflections. These subsequent studies aim to provide a more extensive insight of the complex interaction between rotating machinery and acoustic modes, ultimately leading to more accurate noise prediction tools for industrial applications.

Acknowledgments

The authors acknowledge Safran Ventilation Systems and in particular, Patrice CAULE, for providing the LP3 fan-OGV module. The authors further recognise the valuable assistance of the Hexagon team at Toulouse, France, specifically Clement LULURGA, concerning the numerical simulations. This work was performed in the framework of the Labex CeLyA (grant number ANR-10-LABX-0060) of the University of Lyon, within the program "Investissements d'Avenir" (grant number ANR-16-IDEX-0005) operated by the French National Research Agency.

References

[1] Eversman, W., and Roy, I. D., "Ducted Fan Acoustic Radiation Including the Effects of Nonuniform Mean Flow and Acoustic Treatments," Tech. rep., NASA Lewis Research Center, 1993.

[2] Roger, M., Moreau, S., and Guédel, A., "Vortex-Shedding Noise and Potential-Interaction Noise Modeling by a Reversed Sears' Problem," *12th AIAA/CEAS Aeroacoustics Conference*, AIAA, Cambridge, MA, 2006.

[3] Tyler, J. M., and Sofrin, T. G., "Axial flow compressor noise studies," *SAE Tech Papers*, 1962. https://doi.org/10.4271/620532.

[4] Kaji, S., and Okazaki, T., "Propagation of sound waves through a blade row: I. Analysis based on the semi-actuator disk theory," *Journal of Sound and Vibration*, Vol. 11, No. 3, 1970, pp. 339–353.

[5] Kaji, S., and Okazaki, T., "Propagation of sound waves through a blade row: II. Analysis based on the acceleration potential method," *Journal of Sound and Vibration*, Vol. 11, No. 3, 1970, pp. 355–375.

[6] Philpot, M. G., "The role of rotor blade blockage in the propagation of fan noise interaction tones," *2nd Aero-acoustics Conference*, AIAA, Hampton, VA, 1975.

[7] Posson, H., and Moreau, S., "Effect of Rotor Shielding on Fan-Outlet Guide Vanes Broadband Noise Prediction," *AIAA Journal*, Vol. 51, 2013, pp. 1576–1592. https://doi.org/10.2514/1.J051784.

[8] Blázquez-Navarro, R., and Corral, R., "Prediction of fan acoustic blockage on fan/outlet guide vane broadband interaction noise using frequency domain linearised Navier–Stokes solvers," *Journal of Sound and Vibration*, Vol. 500, 2021, p. 116033.

[9] Adhikary, M., Pereira, A., Jacob, M., Blázquez-Navarro, R., and Thisse, J., "Experimental investigation of rotor shielding effects on axial flow fan using an interstage array," *11th EAA Annual European Conference on Acoustics and Noise Control Engineering*, European Acoustics Association, Sociedad Española de Acústica, Malaga, Spain, 2025.

[10] Mosson, A., Binet, D., and Caprile, J., "Simulation of the Installation Effects of the Aircraft Engine Rear Fan Noise with ACTRAN/DGM," *20th AIAA/CEAS Aeroacoustics Conference*, AIAA, Atlanta, GA, 2014. https://doi.org/https://doi.org/10.2514/6.2014-3188.

[11] Seiner, J. M., and Reethof, G., "Design and Development of the Spinning Mode Synthesizer," Tech. rep., NASA, WASHINGTON, D. C., April 1973.

[12] Huang, S., Pan, X., Yu, L., and Jiang, W., "Achieving cylindrical duct modes generation in spinning mode synthesizer via a least-square identification of the global calibration factor," *Applied Acoustics*, Vol. 186, 2022. https://doi.org/https://doi.org/10.1016/j.apacoust.2021.108423.

[13] Free Field Technologies, *Actran 2023.2 User's Guide: Installation, Operations, Theory and Utilities*, Hexagon AB, Mont-Saint-Guibert, Belgium, 2023. Software Documentation.

[14] Chevaugeon, N., Remacle, J.-F., Gallez, X., Ploumans, P., and Caro, S., "Efficient Discontinuous Galerkin Methods for solving acoustic problems," *11th AIAA/CEAS Aeroacoustics Conference*, AIAA, Monterey, CA, 2005. https://doi.org/https://doi.org/10.2514/6.2005-2823.

[15] Cambier, L., Heib, S., and Plot, S., "The Onera elsA CFD Software: Input from Research and Feedback from Industry," *Mechanics & Industry*, Vol. 14, No. 3, 2013, pp. 159–174. https://doi.org/https://doi.org/10.1051/meca/2013056.

[16] Smith, B. R., "A near wall model for the k-l two equation turbulence model," *25th Fluid Dynamics Conference*, AIAA, Colorado Springs, CO, 1994. https://doi.org/https://doi.org/10.2514/6.1994-2386.

[17] *Mumps: a multifrontal massively parallel sparse direct solver*, Mumps Technologies, 2026.

[18] Pereira, A., and Jacob, M., "Modal analysis of in-duct fan broadband noise via an iterative Bayesian inverse approach," *Journal of Sound and Vibration*, Vol. 520, 2022, p. 116633. https://doi.org/https://doi.org/10.1016/j.jsv.2021.116633.

[19] Munjal, M. L., *Acoustics of ducts and mufflers: with application to exhaust and ventilation system design*, 1st ed., Wiley-Interscience, 1987.

[20] Law, T., Corral, R., Fernández, J., and Serrano, A., "Linear Viscous Eigenmode Analysis Within a Radially Varying Swirling Flow," *16th AIAA/CEAS Aeroacoustics Conference*, AIAA, Stockholm, Sweden, 2010. URL https://doi.org/10.2514/6.2010-3890.